

Cite this: *Analyst*, 2012, **137**, 2791[www.rsc.org/analyst](http://www.rsc.org/analyst)

PAPER

# The optimisation of facile substrates for surface enhanced Raman scattering through galvanic replacement of silver onto copper†

Samuel Mabbott,<sup>a</sup> Iain A. Larmour,<sup>b</sup> Vladimir Vishnyakov,<sup>c</sup> Yun Xu,<sup>a</sup> Duncan Graham<sup>b</sup> and Royston Goodacre<sup>\*a</sup>

Received 7th March 2012, Accepted 3rd April 2012

DOI: 10.1039/c2an35323g

A fast and cost-effective approach for the synthesis of substrates used in surface enhanced Raman scattering (SERS) has been developed using galvanic displacement. Deposition of silver onto commercially available Cu foil has resulted in the formation of multiple hierarchical structures, whose morphology show dependence on deposition time and temperature. Analysis of the surface structure by scanning electron microscopy revealed that the more complex silver structures correlated well with increased deposition time and temperature. Using Rhodamine 6G (R6G) as a model Raman probe it was also possible to relate the substrate morphology directly with subsequent SERS intensity from the R6G analyte as well as the reproducibility across a total of 15 replicate Raman maps (20 × 20 pixels) consisting of 400 spectra at a R6G concentration of 10<sup>−4</sup> M. The substrate with the highest reproducibility was then used to explore the limit of detection and this compared very favourably with colloidal-based SERS assessments of the same analyte.

## Introduction

An increasing amount of interest is being invested in the development of metallic nanostructures due to their potential applications in catalysis, biomedicine, information storage and sensing.<sup>1–5</sup> Coinage metals such as copper, gold and silver have shown a huge amount of potential and are useful in ultra-trace biological and chemical sensing, surface plasmon resonance (SPR) and surface enhanced Raman scattering (SERS).<sup>6–10</sup> A substantial amount of time and effort has also been centred on the modification of synthetic strategies that provide the desired control over nanostructure morphology. Commonly applied methods of synthesis include photochemical reactions,<sup>11</sup> use of templates,<sup>12</sup> seed-mediated growth,<sup>13</sup> electrochemical deposition,<sup>14,15</sup> ultrasonic-assisted template methods<sup>16,17</sup> and surfactant/organic molecule assisted reduction/stabilisation.<sup>18,19</sup> Development of these methodologies has allowed the creation of nano-metallic rods,<sup>20,21</sup> chains,<sup>22</sup> cubes,<sup>23</sup> wires,<sup>24</sup> plates,<sup>25</sup> spheres,<sup>26</sup> stars<sup>27</sup> and dendrites.<sup>28</sup> However many of the synthetic

techniques are either labour intensive and/or necessitate the use of expensive instrumentation. Two highly desirable properties of SERS substrates are the creation of areas of high enhancement with the concomitant ability to tune the localised surface plasmon resonance of the nanostructures. A readily accessible technique that can achieve this is galvanic displacement (GD)<sup>29–31</sup> which also offers the option of nanostructural growth on an appropriate substance in an extremely efficient, facile and rapid way. This electroless plating technique has been reported for Au on Si, Cu on Si, Zn on Al and multiple other combinations.<sup>32–34</sup> Our focus of galvanising Cu using Ag has very recently been reported and the resultant structures from this readily accessible synthesis have been suggested as an effective process for the production of SERS substrates.<sup>35,36</sup>

As a result of the difference in electric potentials between the silver solution and copper foil, deposition can occur very quickly, which although promoting anisotropic growth is favourable in the development of a SERS substrate because of increased particle aggregation and hence, the formation of high enhancement areas. Another aspect of GD which is favourable for SERS is the ability to tune the nanostructures' optical properties. The origin of these properties is a phenomenon known as localised surface plasmon resonance (LSPR). When these roughened metal surfaces are irradiated with light delocalised electrons (plasmons) collectively oscillate relative to the lattice of positive nuclei and couple to the photon to create a new quasi-particle known as a plasmon polariton.<sup>29</sup> For the coupling to occur it is essential that the plasmons oscillate at a frequency which is close to that of the incident light. It has been demonstrated that shape and

<sup>a</sup>School of Chemistry, Manchester Interdisciplinary Biocentre, University of Manchester, 131 Princess Street, Manchester, UK. E-mail: roy.goodacre@manchester.ac.uk

<sup>b</sup>Centre for Molecular Nanometrology, WestCHEM, Department of Pure and Applied Chemistry, University of Strathclyde, 295 Cathedral Street, Glasgow, UK

<sup>c</sup>Surface Coating and Characterisation Research Group, Department of Chemistry and Materials, Manchester Metropolitan University, Chester Street, Manchester, UK

† Electronic supplementary information (ESI) available. See DOI: 10.1039/c2an35323g

geometry controlled synthesis of these nanostructures is a versatile route in the tuning of the LSPR peak position across the visible and NIR spectral regions.<sup>29</sup> In much of the earlier work on silver or gold substrates, fabrication has involved the immobilisation of colloidal nanoparticles onto solid platforms such as glass or quartz. These metals are often bound to the surface *via* a functionalised silane linker or polymer.<sup>37,38</sup> Apart from the syntheses of these substrates being laborious, signals from the organic molecules used in the linking or reduction/stabilisation of the nanoparticles can repeatedly result in the existence of background signal, making the spectral signature of the analyte very difficult to resolve. Furthermore the coupling between the particles (close vicinity) is important for the presence of a hot spot, not their monodispersity. Here we have exploited the difference in electrode potentials to fabricate substrates in which the Ag<sup>+</sup> ions have spontaneously replaced Cu atoms through GD. For the reaction to proceed the metal with the higher electrode potential must be in solution. In our case Ag<sup>+</sup>/Ag possesses a potential of +0.799 V (SHE) where as Cu<sup>2+</sup>/Cu has a potential of +0.337 V (SHE) so the AgNO<sub>3</sub> is contained in solution. The full and half equations for this reaction are displayed in Scheme S1†.

Differences in the structure of the silver surface can be produced by modifying the concentration of the silver solution, heating the solution or changing the deposition time. This can also have a profound effect on the enhancement of the Raman signal arising from the analyte. As concentration effects have been extensively explored our focus is on how the alteration of deposition time and temperature affects the reproducibility and enhancement of R6G. The probe analyte Rhodamine 6G (R6G) has been chosen because of its problematic fluorescence in the absence of a SERS substrate and its widespread use in SERS as a test analyte.<sup>39</sup> Much of the past optimisation work has revolved around the theorisation of synthetic strategies to produce surfaces with the best SERS response, here optimisation is carried out on the basis of spectroscopic results, which are presented in an unbiased and raw manner.

## Experimental

### Materials

Silver nitrate (99.999%) and trisodium citrate were purchased from Sigma Aldrich (Dorset, UK). Copper foil (1 mm thickness) was obtained from a commercial retailer. All solvents used throughout the synthesis were of analytical grade.

### Synthesis of optimal silver on copper (SoC) surface

Copper foil was cut into 2.5 cm × 7.5 cm strips and fixed to a standard microscope slide to generate a more rigid surface. The Cu surface was then cleaned with copious amounts of methanol followed by acetone. 10 µL of 0.1 M AgNO<sub>3</sub> solution was then spotted onto the surface and left to develop for a specified time. Deposition of the nanoparticles was signified by the formation of a grey target on the copper foil. Post deposition, further surface cleaning was carried out using deionised water to remove any residual silver nitrate reagent and copper nitrate product. The substrate was then dried under a stream of nitrogen.

### Synthesis of silver nanoparticles

All glassware was cleaned using aqua regia [nitric acid : hydrochloric acid (1 : 3, v/v)]. This was performed to remove any trace metals, which may be residing in the glassware. After an hour of treatment the flasks were then scrubbed with soap and rinsed with deionised water (18.2 Ω). The flasks were then left to dry in a 50 °C oven for 20 min. Silver nanoparticles were synthesised using the Lee and Meisel method.<sup>40</sup> Briefly, AgNO<sub>3</sub> (90 mg) was dissolved in 500 mL of water and brought to the boil. A solution of 1% trisodium citrate (10 mL) was added. The solution was then left on a steady boil for 1 h. The reaction was deemed to have reached its end point once the solution had a milky green hue.

### UV-visible (UV-vis) absorption/extinction nanoparticle characterization

Silver nanoparticles synthesised by citrate reduction were characterised using UV-visible spectroscopy to determine the surface plasmon band  $\lambda_{\text{max}}$  of the nanoparticles. In order for the absorbance values to be less than 1 it was necessary to dilute the sol 1 part in 9 parts water. 1 mL of the diluted nanoparticle solution was then placed into a quartz cuvette and inserted into the sample holder of a Thermo Biomate 5 (Thermo Fisher Scientific Inc., Massachusetts, USA). An absorption/extinction spectrum was collected over a range of 300 to 800 nm. The silver sol was shown to have a surface plasmon band  $\lambda_{\text{max}}$  of 421 nm, which is characteristic of silver colloids synthesized using the Lee and Meisel method.<sup>41</sup>

### Scanning electron microscopic (SEM) and energy dispersive X-ray analysis (EDX)

SEM allows for the accurate determination of nanoparticles size and shape distributions in a sol and also helps in the tracking of morphological changes at the copper–silver interface created using GD. For the imaging of nanoparticles synthesized in solution, 10 µL of the sol was spotted onto a silicon slide and left to dry for 24 h. Microscopic analysis of the SoC slides was carried out on the silver targets deposited as described in the synthesis. SEM analysis of the SoC substrates was carried out using a Zeiss Supra 40 VP field-emission gun scanning electron microscope (FEG-SEM; Carl Zeiss SMT GmbH, Oberkochen, Germany) operating at a voltage of 3 kV, imaging of the silver sol was carried out at a voltage of 1 kV. The SEM is also equipped with an EDX instrument (EDAX Inc., New Jersey, USA) which was used to identify the elemental composition of selected substrates. Here EDX was used to verify that silver had been deposited onto the copper surface.

### Preparation of SoC substrates for Raman mapping

For the exploration of temporal effects on the silver deposition and relative analyte signal, the length at which the silver solution was applied to the surface for was altered. Effects of deposition time were examined at 10 s, 20 s and 30 s. Once the optimum deposition period had been identified it was then used to explore temperature effects. Silver nitrate was spotted onto the copper surface at room temperature (RT = ~23 °C), 30 °C, 40 °C, 50 °C,

60 °C, 70 °C, 80 °C, 90 °C and 100 °C. For the Raman optimisation of the substrates 1  $\mu$ L of a  $10^{-4}$  M methanolic R6G solution was spotted onto the silver deposition site and left to air dry. Once the most reproducible substrate had been identified it was used to establish the limit of detection of R6G.

### Raman mapping

Raman analyses were undertaken using a WITec Alpha 300R confocal Raman instrument (WITec GmbH, Ulm Germany) fitted with a piezo-driven XYZ scan stage. All samples were probed using a laser wavelength of 632.8 nm. The grating was 600 g mm $^{-1}$  and coupled to a thermoelectrically cooled charge-coupled device (CCD). A spectral resolution of 2.7 cm $^{-1}$  was achieved over a spectral width consisting of 1024 pixels spanning from 130–2900 cm $^{-1}$ . The unfocused laser power at the sample was measured at  $\sim$ 1.0 mW. Spectra were acquired across an area measuring 20  $\mu$ m  $\times$  20  $\mu$ m using an Olympus 50 $\times$ /0.5 objective. 20 points per line and 20 lines per image were recorded to give a spatial resolution of 1  $\mu$ m. Each spectrum had an integration time of 0.08 s. Five replicate maps were taken on each of the three substrates, resulting in 15 maps being obtained at each optimization parameter. Background spectra of all the synthesized silver targets were acquired before maps were collected on the R6G deposited surfaces. All data used in the analysis were collected from in and around the silver targets centre to avoid any data discrepancies that could occur from mapping at the areas at the target edges. In order to show that the enhancement was purely obtained from the silver target one exemplar map has been generated at silver deposition area and copper interface (see discussion below).

### Colloidal-based SERS in solution

Spectra were collected using a DeltaNu Advantage benchtop Raman spectrometer (Intevac inc, California, USA). The instrument is equipped with a 632.8 nm HeNe laser with a power output of 3 mW. Spectra were collected for 5 s over a range of 200–3400 cm $^{-1}$  at a spectral resolution of 10 cm $^{-1}$ . Solution samples were placed in an 8 mm diameter glass vial and subjected to laser irradiation once loaded into the sample cell attachment. The instrument was calibrated to determine the ideal distance from the laser to the glass vial using toluene and polystyrene. In a typical SERS interrogation 200  $\mu$ L of aqueous R6G was added to 200  $\mu$ L of silver sol along with 50  $\mu$ L of 0.5 M KNO $_3$  aggregating agent. The vial was then vortexed for 5 s and inserted into the sample cell attachment where a spectrum was acquired immediately.

## Results and discussion

### Characterisation of substrates

During galvanic displacement it was observed that the silver nanocrystals deposited on the surface of the copper display an array of morphologies that appeared to be dependent on deposition time and temperature. In Fig. 1, the representative SEM images show a selection of these deposits where it can be observed that when the silver nitrate solution was left to develop for longer time periods on the surface of the copper the more elaborate the deposition morphologies became. The blank copper surface can be seen to be fairly smooth with only a few

sites on the surface displaying indentations or roughness. The galvanic displacement reaction takes place extremely quickly, so when the silver nitrate solution was applied onto the surface for only 10 s there was an appreciable deposition and growth of silver nanocrystals across the copper. A maximum deposition time of 30 s was chosen because of the difficulty in washing off any excess silver nitrate or newly formed copper nitrate solution without stripping the silver crystals from the copper surface. At 30 s the size of the silver deposits increases rapidly and the morphologies differ greatly. Crystalline deposits with diameters of  $\sim$ 2  $\mu$ m were observed at 30 s deposition time as well as dendritic deposits and nanoparticle clusters. Spotting of the AgNO $_3$  solution on the copper surface at differing temperatures also yielded varying effects. As the temperature was increased so did the complexity of the silver deposits. When the silver was applied at RT only single and clustered nanoparticles were formed. At a mid-range temperature of 60 °C bigger crystalline deposits could be observed along with the initial formation of dendrites as observed when the deposition was carried out at RT for 30 s. By contrast, at the maximum deposition temperature of 100 °C the surface was completely covered in the silver dendritic structures. It can be concluded from these SEM images that the growth of silver deposits at the copper interface is anisotropic with extremes of temperature or time inducing the growth of much more heterogeneous and complex structures. The formation of Ag dendrites has previously been observed in galvanic displacement-type reactions and the diffusion limited aggregation model justifies their synthesis.<sup>42</sup> Previously it has also been shown that trunks and branches grow along the  $\langle$ 211 $\rangle$  direction and the leaves grow along  $\langle$ 111 $\rangle$  direction of the cubic *Fm3m* structure, leading to the formation of dendrites.<sup>43</sup>

To investigate the coverage of silver on the surface at a variety of experimental temperatures and times, energy dispersive X-ray analysis was carried out. The results of the EDX analyses are summarised in Table S1†. Although it is not possible to derive clear compositional data from EDX analysis it can be revealed that the particles, plates and dendritic structures which appear at the target sites are indeed composed of silver. No great variation in the elemental composition of the substrate was observed. The surface that was synthesised for 30 s at RT shows a slight drop in the % Ag and an increase in % Cu but as previously discussed this could be due to silver mass lost through the washing cycle. The low % O weight at the surface is also promising as oxidation of the silver nanostructures has been shown to hinder SERS.<sup>44</sup>

### Proof of SERS activity

To demonstrate that the SERS effect was only arising from the silver surface R6G ( $1 \times 10^{-4}$  M) was spotted across the silver–copper interface and mapped. The mapping parameters used were as described previously except the area mapped was extended to 80  $\mu$ m  $\times$  80  $\mu$ m. The optical image, heat map and Raman spectra representative of signals arising from the silver and copper surface are shown in Fig. 2. The optical image clearly defines the interface between the silver deposition site (red dot) and copper surface (blue dot). The heat map was generated using the baseline corrected peak area of the R6G peak at 1368 cm $^{-1}$ , which is characteristic of the combined C–C and C–N stretches (see Table in Fig. 2). The signal at 1368 cm $^{-1}$  is only visible on the

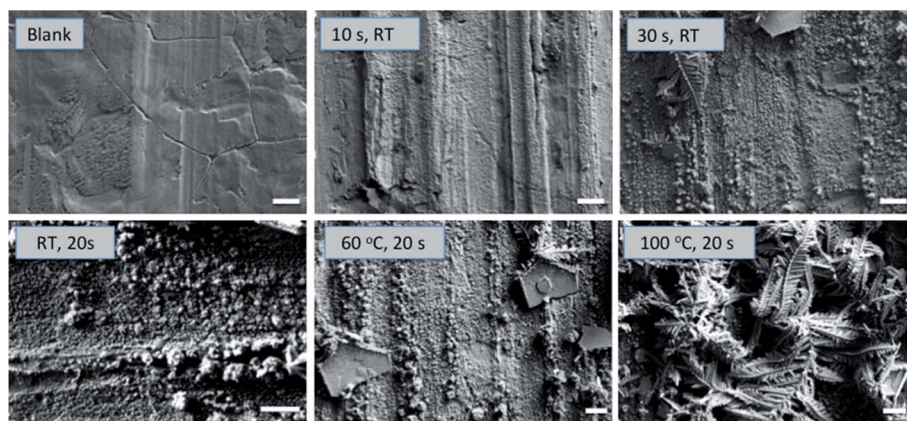


**Fig. 1** SEM images taken of the silver on copper (SoC) substrate at a range of deposition times and temperatures. The top row of images show the blank copper surface and the surface after silver nitrate deposition times of 10 s and 30 s at room temperature (RT  $\approx$  23 °C). The temporal evolution of the substrate shows more complex structure formation occurs when the silver nitrate is left to mature on the surface for longer time periods. The image taken after 30 s of GD time show the formation of large nanoparticles, nanoplates and dendrites. The bottom row of SEM images display the effect of deposition temperature on the morphology of silver on the surface of the copper. At RT silver nanocrystals are formed on the copper surface and show a great affinity for clustering. At 60 °C the clustering of the silver particles is still present however, there is also evidence for the formation of nanoplates and dendrites. By contrast at 100 °C the surface solely consists of dendritic silver structures. The white scale bar in the bottom right hand corner of each image corresponds to a distance of 1  $\mu$ m.

surface where the silver has been deposited and not on the copper, thus proving that the GD of silver is SERS active, and that smooth Cu is not generating any SERS effect. The spectra shown were generated by averaging 10 random spectra taken from in and around the areas represented by the red and blue dots, these reinforce the fact that signal only arises from the R6G which is present on the silver target whilst the spectra acquired from sites on the copper display background noise only.

### Optimisation of deposition time

To generate substantial and comparable datasets three replicate SoC substrates were produced at each time point (9 targets in total). Once synthesised R6G was applied immediately to each of the surfaces; generally the time between the substrate being synthesised and the conclusion of the Raman mapping was around 1 h. The intensity values for each of the 400 spectra and the Raman shift values present in each map were extracted using the WITec software. The 45 maps were then individually imported into Matlab (MathWorks, Cambridge, UK) and reshaped to represent a data matrix whose rows and columns consisted of data points and Raman intensity respectively. Plots of the raw R6G spectra were visualised and six characteristic R6G peaks were selected at 619  $\text{cm}^{-1}$ , 778  $\text{cm}^{-1}$ , 1324  $\text{cm}^{-1}$ , 1368  $\text{cm}^{-1}$ , 1513  $\text{cm}^{-1}$  and 1650  $\text{cm}^{-1}$  for further scrutiny. Fig. 2 details the peaks and their archetypal vibrations and Fig. 2D demonstrates an example of a R6G SERS spectrum collected from a SoC surface with the individual peaks annotated. It is also important to mention that data pre-processing was kept to a minimum in order to preserve as much raw nature of the spectra as possible; this also means that similar data analysis methods could easily be applied to alternative substrates.

Each of the peaks were manually assigned a start and end point (Fig. 2). These points were used to extract peak data from each map. Extracted peaks were baseline corrected making sure that the peak minima had a  $y$  value of zero in order to eliminate any

background signal that could affect any subsequent analysis. There are two common ways of measuring a peak: one method requires only the intensity at the peak maxima to be procured, whilst the second approach involves the calculation of the peak area. Although both methodologies have been used here to produce comparable correlation data, peak area is preferred as the estimated value relates not only to the intensity of the peak but also the peak morphology. Peak area was calculated using a trapezoidal integration method available within Matlab. An average of the peak area values and percentage relative standard deviation (%RSD) was taken for the six peaks on each of the 45 maps. A global average of the mean and %RSD was calculated for each time variable (15 maps). The global values were then used for optimisation purposes. The data in Table 1 show that for peaks 1 and 6 there is a negative correlation between the average peak area of Raman signal observed on the surface and the increase in deposition time. However, for peaks 2, 3, 4 and 5 a deposition time of 20 s produces around a 14% average increase in Raman intensity when compared to the second best deposition of 10 s. An increased deposition time of 30 s results in a dramatic decrease in the Raman signal with peaks at 1399  $\text{cm}^{-1}$  and 1554  $\text{cm}^{-1}$  displaying a negative mean peak area value showing they were not observed at all. Again the reduced Raman enhancement effect and subsequent high %RSDs observed at 30 s could be due to the loss of silver during the washing cycle. Different washing methods were used to try to reduce the loss of silver at the surface but they produced similar results to the ones observed in Table 1 (data not shown). Analysis of the %RSD values clearly shows that a 20 s deposition time favours reproducibility of signal across the surface, therefore this deposition time was used to explore the optimisation of deposition temperature.

### Optimisation of deposition temperature

The collection and analysis of Raman data for the 6 selected peaks was carried out in exactly the same way as for the

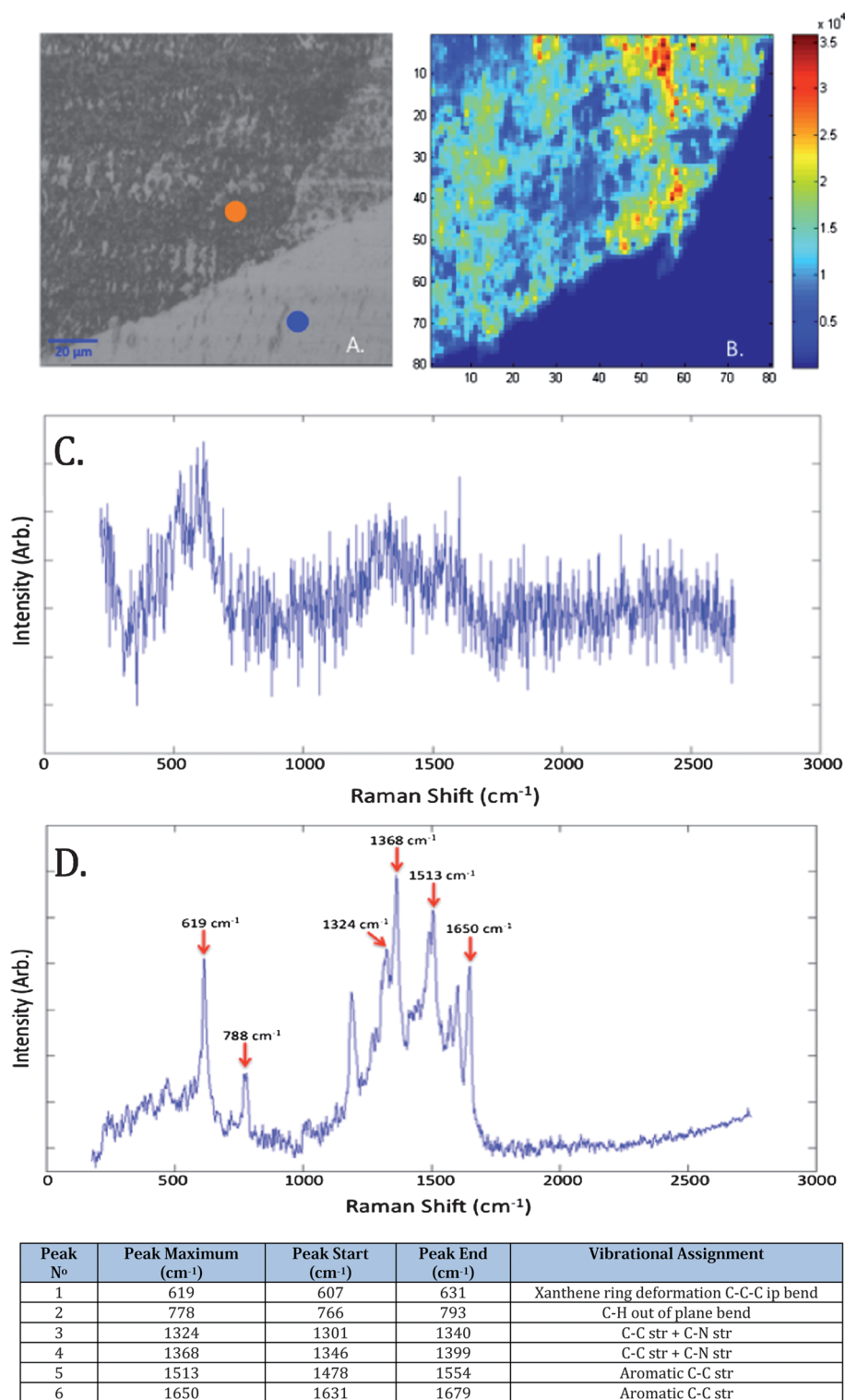


**Fig. 2** (A) Optical image showing the area on the border of the silver deposition area (red dot) and copper that was mapped (blue dot). (B) Corresponding heat map generated by integrating under the R6G peak present at  $1368\text{ cm}^{-1}$ . The spectrum displayed in (D) is representative of Rhodamine 6G spectra acquired on the silver surface, whilst spectrum (C) represents spectra acquired on the background copper surface. Both (D) and (C) are the direct result of averaging 10 spectra taken from the areas highlighted by the red and blue dots. The table displays the six peaks used for data analysis.

optimisation of deposition time (Fig. 3). However, there were 9 variables (RT, 30–100 °C in 10 °C steps). It was observed that the average mean peak area generally increases with an increase in temperature. However the %RSD is at its lowest for all peaks

except peak 6 when the deposition of silver at the surface is carried out at RT. To demonstrate the trends shown by the mean and %RSD with increasing temperature a correlation coefficient ( $r$ ) was calculated (Table 2). The correlation coefficient is



**Table 1** Global averages for R6G peak intensities from Raman maps ( $20 \times 20$  pixels) including all 400 spectra with corresponding %RSDs for each peak at the three deposition times investigated

	Peak 1		Peak 2		Peak 3		Peak 4		Peak 5		Peak 6	
Deposition time (s)	Average mean	Average %RSD	Average mean	Average %RSD	Average mean	Average %RSD	Average mean	Average %RSD	Average mean	Average %RSD	Average mean	Average %RSD
10	2426.6	145.3	1472.3	151.5	1464.8	173.9	4956.9	150.7	4799.8	165.9	5028.8	152.1
20	2311.0	55.0	1675.7	54.4	2055.8	58.3	5129.9	56.60	5550.3	61.8	4134.5	57.7
30	111.8	131.2	246.5	305.4	471.2	104.8	−1361.7	−142.4	−1623.3	−218.8	3290.3	97.8

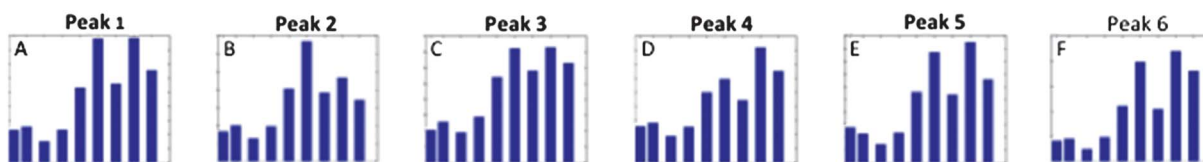
a measure of the strength of the linear relationship of two variables in this case temperature and relative peak area means and %RSDs. If the  $r$  value is close to either 1 or  $-1$  then a relationship between the experimental and calculated variables is demonstrated, however a value close to 0 means that there is no linear relationship present. The majority of peaks show a %RSD correlation value of  $>0.79$  except for peak 6 which has a %RSD of 0.38 meaning that an increase in temperature mainly results in an increase in %RSD. It is believed that the %RSD and mean show excellent correlation with the structural morphology of silver deposited on the copper surface. Images acquired on the SEM show a relatively non-complex homogeneous deposition of silver nanocrystals at  $23^\circ\text{C}$ , because of the homogeneity, the signal arising from the R6G is much less variable when compared to the increased RSDs when silver is deposited at a higher temperature. At  $100^\circ\text{C}$  we see that the substrate consists of only dendritic silver, whose complex structural morphology produced by anisotropic growth has been reported before albeit synthesised using different reaction conditions.<sup>45,46</sup> The morphology and SERS response of the dendrites fit the model proposed by Garcia-Vidal and Pendry,<sup>47</sup> which explains that more compact particles have a much stronger SERS effect than isolated particles. However the increased SERS effect of silver deposited at a higher temperature as shown in Fig. 4 *via* the positive correlation coefficients is not without its caveat of increased %RSD values. Overall the substrates synthesised at RT demonstrated

a lower %RSD because of their less complex, more homogeneous structural morphology. The SoC substrate synthesised at  $90^\circ\text{C}$  demonstrated the greatest SERS enhancement effects. Analysis of the averaged means of each peak and respective %RSDs was also carried (Table 2) out using the intensity recorded at the peak maxima instead of peak area. Comparison of peak intensity and peak area data shows no major differences in correlation coefficient values meaning neither method of spectral analysis in this case can be preferred over the other.

#### Establishing the LOD of R6G on the SoC substrates

A methanolic solution of Rhodamine 6G was applied to the SoC substrates at serial dilutions varying from  $1 \times 10^{-4}$  M to  $1 \times 10^{-8}$  M. Three  $20 \times 20 \mu\text{m}$  Raman maps were collected on three replicate SoC substrates at each concentration resulting in the generation of 3600 spectra in total. Limit of detection (LOD) analysis was carried out on the raw data, baseline corrected data, 6-peak spectra (consisting only of the recombined extracted peaks) and on the individual peaks. Morphological scores (MS) were used to filter out any non-R6G spectra. MS is a multivariate extension of the signal-to-noise ratio and is designed to separate a relatively smooth sequence of signals with structural information (*e.g.*, a Raman spectrum with multiple bands) from the signals full of random variations (*i.e.*, noise). A high MS implies a smooth sequence with the major variance in the low frequency

#### Mean Peak Area



#### Mean %RSD

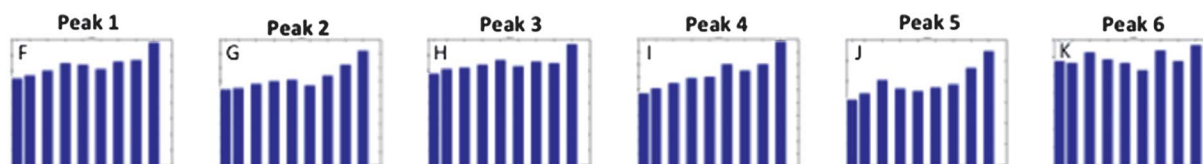


**Fig. 3** The global averages calculated for the peaks 1–6 (A–F) at each optimisation temperature ( $23$ – $100^\circ\text{C}$ ) are displayed on the top row. The  $x$  axes underneath each of the bars represents the temperatures whilst the maximum height for peaks 1–6 are: (A) 9000, (B) 7000, (C) 8000, (D) 18 000, (E) 20 000 and (F) 25 000. The bottom row of plots represent the %RSDs of each peak. The maximum height of each of the respective peaks 1–6 are: (F) 80, (G) 90, (H) 80, (I) 100, (J) 120 and (K) 70.

**Table 2** Correlation coefficients for the mean and %RSD for each peak in the R6G spectra with respect to temperature. Two datasets were generated and are compared from both peak areas and intensities

Peak area	Peak 1	Peak 2	Peak 3	Peak 4	Peak 5	Peak 6
<i>R</i> (mean)	0.82	0.65	0.89	0.86	0.80	0.85
<i>R</i> (%RSD)	0.88	0.87	0.79	0.94	0.81	0.38
Intensity	Peak 1	Peak 2	Peak 3	Peak 4	Peak 5	Peak 6
<i>R</i> (mean)	0.87	0.73	0.89	0.88	0.87	0.86
<i>R</i> (%RSD)	0.90	0.83	0.78	0.96	0.86	0.54

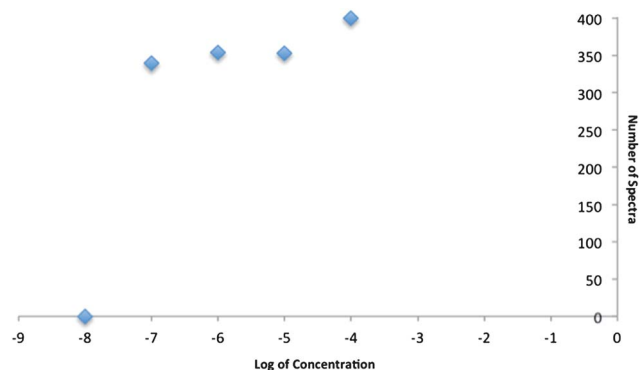


**Fig. 4** Plot showing the average number of R6G spectra observed on the optimised SoC substrate at each of the concentrations ( $1 \times 10^{-4}$  M to  $1 \times 10^{-8}$  M) when a  $MS > 2$  threshold is applied. The concentrations are displayed as  $\log_{10}$  values.

domain which normally is what a chemical spectrum represents. By contrast, a low  $MS$  implies a sequence with its major variations in the high frequency domain which normally means noise.<sup>48</sup> Although it is appreciated that the molecules of R6G may adopt different orientations on the surface of the silver thus causing a variation in signal,  $MS$  allows the large datasets to be quickly filtered. After applying a threshold of 2 to all the dataset

variants it was decided that the 6 peak plot best represented the R6G signal at the surface and that at this threshold any unwanted noise was removed; an example of the filtering is shown in Fig. S1†. Using the applied threshold the number of spectra relating to R6G Raman vibrations was calculated for each map. The values for each map were then averaged to obtain a global average for each concentration, the plot shown in Fig. 4 displays this relationship and shows that the LOD is  $10^{-7}$  M.

### SoC substrate vs. silver colloid in solution

To compare the detection limit of R6G on the SoC substrate with solution-based colloidal SERS, silver citrate colloids were produced using the well documented and characterised Lee and Meisel methodology. SEM images of the colloids (data not shown) revealed nanoparticles with aspect ratios differing between 1 : 1 to 1 : 5 with the average particle size being between 50 and 100 nm. For LOD analysis an aqueous solution of R6G at a concentration of  $1 \times 10^{-4}$  M was serially diluted down to  $1 \times 10^{-9}$  M. Three replicate spectra were generated at each concentration. Univariate and multivariate methods were used to establish the limit of detection. For univariate analysis the six peaks relating to R6G vibrations outlined earlier were extracted and baseline corrected. The peak area for each replicate was calculated and the mean peak area and standard deviation (SD) was established for each concentration. Fig. S2A† shows the mean spectra at each concentration and also displays the aggregated silver nanoparticle blank. The overlaid spectra in Fig. S2B† shows the mean spectra at  $10^{-4}$  M,  $10^{-5}$  M,  $10^{-6}$  M and  $10^{-7}$  M R6G concentrations and Fig. S2C† shows an example peak extraction and baseline correction. The limit of detection is defined as  $3 \times SD$  and based on peaks 1, 5 and 6 the LOD was established as  $10^{-7}$  M, a summary of the results can be seen in Table S2†. Principal components analysis (PCA)<sup>49</sup> was also carried out on the dataset to see if multivariate methods revealed a similar LOD. Fig. 5 shows the PCA scores plot with PC1 identifying 95.7% of the total explained variance in the dataset. The separation across PC1 is relative to concentration with

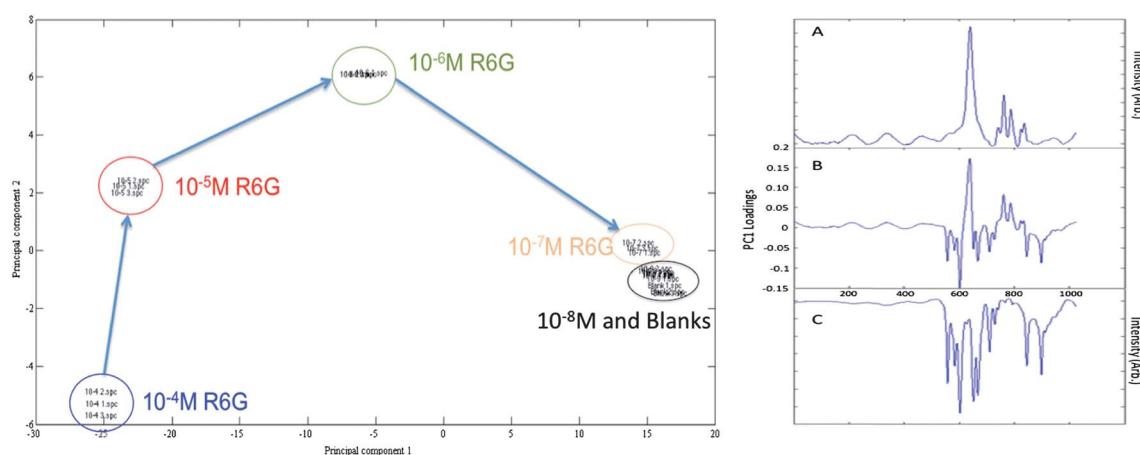


**Fig. 5** The PCA scores plot to the left shows how the different concentrations of R6G cluster; the ellipses are shown as a guide and have no statistical meaning. The LOD was established as  $10^{-7}$  M as it clusters separately from the blanks whilst  $10^{-8}$  M overlaps with the blank spectra. The loading plot representative of separation across PC1 is displayed on the right. The spectrum in (A) is that of a silver colloidal blank and accounts for the positive values seen in the loadings, whilst (C) is a SERS spectrum of R6G and is accountable for the negative values in PC1.

$10^{-4}$  M being represented on the far left and  $10^{-8}$  M,  $10^{-9}$  M and blanks on the far right. It is also evident that whilst  $10^{-7}$  M is to the right of the PCA plot it is separate from the lower concentrations and the blanks so this was taken as the LOD. Hence, it can be deduced that both univariate and multivariate methodologies show corroborative results and the LOD for R6G is  $10^{-7}$  M. Analysis of the PC1 loadings plot (Fig. 5) shows how the positive values are representative of the silver colloidal blanks whilst the negative values represent the SERS spectrum of Rhodamine 6G. Thus the LOD for colloidal SERS and SoC surfaces is in agreement at  $10^{-7}$  M for R6G.

## Concluding remarks

The synthesis of SERS active silver substrates *via* galvanic displacement is quick and facile allowing the technique of SERS to be exploited in groups with little experience of nanoparticle production. We have successfully shown that even heterogeneous silver structures give rise to huge Raman enhancement and suppression of fluorescence effects otherwise present in Rhodamine 6G Raman spectra. It has also been shown that by manipulating temperature and temporal variables it is possible to optimise the surface with regards to analyte signal intensity and %RSDs, both of these values have also been represented here as an average of all spectra taken without any filtering so they truly reflect the performance of the substrates over the whole map area generated ( $20 \times 20$  pixels). Using the 'optimised' substrate it was then possible to establish the limit of detection of Rhodamine 6G as being  $1 \times 10^{-7}$  M from these surfaces which was comparable to the detection of R6G in solution using a standard colloidal preparation.

## Acknowledgements

The authors thank the RSC and EPSRC for funding SM's Analytical Studentship and the EU Single Molecule Detection project for funding to IL. DG acknowledges the Royal Society for the award of a Wolfson Research Merit award.

## References

- 1 Y. G. Sun, C. H. Lei, D. Gosztola and R. Haasch, *Langmuir*, 2008, **24**, 11928.
- 2 S. Guo, S. Dong and E. Wang, *Eur. J. Chem.*, 2008, **14**, 4689.
- 3 V. Bansal, A. P. O'Mullane and S. K. Bhargava, *Electrochem. Commun.*, 2009, **11**, 1639.
- 4 C. H. Wang, D. C. Sun and X. H. Xia, *Nanotechnology*, 2006, **17**, 651.
- 5 J. Chen, B. Wiley, J. McLellan, Y. Xiong, Z. Y. Li and Y. Xia, *Nano Lett.*, 2005, **5**, 2058.
- 6 Y. L. Wang, P. H. C. Camargo, S. E. Skrabalak, H. C. Gu and Y. N. Xia, *Langmuir*, 2008, **24**, 12042.
- 7 X. G. Hu and S. J. Dong, *J. Mater. Chem.*, 2008, **18**, 1279.
- 8 C. L. Lee and C. M. Tseng, *J. Phys. Chem. C*, 2008, **112**, 13342.
- 9 J. Sharma, Y. A. Tai and T. Imae, *J. Phys. Chem. C*, 2008, **112**, 17033.
- 10 J. Y. Chen, B. J. Wiley and Y. N. Xia, *Langmuir*, 2007, **25**, 4120.
- 11 R. He, X. F. Qian, J. Yin and Z. K. Zhu, *Chem. Phys. Lett.*, 2003, **369**, 454.
- 12 Z. Wang, F. Tao, D. Chen, L. Yao, W. Cai and X. Lei, *Chem. Lett.*, 2007, 672.
- 13 S. L. Smitha, K. G. Gopchandran, T. R. Ravindran and V. S. Prasad, *Nanotechnology*, 2011, **22**, 265705.
- 14 Q. Zhao, S. Wang, N. Jia, L. Liu, J. Yang and Z. Jiang, *Mater. Lett.*, 2006, **60**, 3789.
- 15 C. D. Geddes, A. Parfenov, I. Gryczynski and J. R. Lakowicz, *J. Phys. Chem. B*, 2003, **107**, 9989.
- 16 J. Xiao, Y. Xie, R. Tang, M. Chen and X. Tian, *Adv. Mater.*, 2001, **13**, 1887.
- 17 J. J. Zhu, S. W. Liu, O. Palchik, Y. Koltypin and A. Gedanken, *Langmuir*, 2000, **16**, 6396.
- 18 T. Ang and W. Chin, *J. Phys. Chem. B*, 2005, **109**, 22228.
- 19 P. S. Mdluli and N. Revaprasadu, *Mater. Lett.*, 2009, **63**, 447.
- 20 J. Fu, Z. Cao and L. Yobas, *Nanotechnology*, 2011, **11**, 505302.
- 21 X. Zhang, Q. Zhou, J. Ni, Z. C. Li and Z. Zhang, *Phys. E*, 2011, **44**, 460.
- 22 D. Zhang, Q. Zhang, L. Niu, L. Jiang, P. Yin and L. Guo, *J. Nanopart. Res.*, 2011, **13**, 3923.
- 23 M. Rycenga, X. Xia, C. H. Moran, F. Zhou, D. Qin, Z. Y. Li and Y. Xia, *Angew. Chem., Int. Ed.*, 2011, **50**, 5473.
- 24 F. Bayata, Z. B. Akinci, A. S. Donatan and M. Urgen, *Mater. Lett.*, 2012, **67**, 387.
- 25 C. Wang, H. Ding, G. Xin, X. Chen, Y. Lee, J. Hao and H. Lui, *Colloids Surf., A*, 2009, **340**, 93.
- 26 Q. Zhang, W. Y. Li, C. Moran, J. Zeng, J. Y. Chen, L. P. Wen and Y. N. Xia, *J. Am. Chem. Soc.*, 2010, **132**, 11372.
- 27 A. Guerrero-Martinez, S. Barbosa, I. Pastoriza-Santos and L. Liz-Marzan, *Curr. Opin. Colloid Interface Sci.*, 2011, **16**, 118.
- 28 S. Lv, H. Suo, X. Zhao, C. Wang, S. Jing, T. Zhou, Y. Xu and C. Zhao, *Solid State Commun.*, 2009, **149**, 1755.
- 29 C. M. Cobley and Y. Xia, *Mater. Sci. Eng., R*, 2010, **70**, 44.
- 30 A. Gutes, C. Carraro and R. Maboudian, *J. Am. Chem. Soc.*, 2010, **132**, 1476.
- 31 W. Song, Y. Cheng, H. Jia, W. Xu and B. J. Zhao, *J. Colloid Interface Sci.*, 2006, **298**, 765.
- 32 H. Suigimura, M. Kanda, T. Ichii and K. Murase, *J. Photochem. Photobiol., A*, 2011, **22**, 209.
- 33 C. Carraro, L. Magagnin and R. Maboudian, *Electrochim. Acta*, 2002, **47**, 2583.
- 34 E. Stoyanova and D. Stoychev, *J. Appl. Electrochem.*, 1997, **27**, 760.
- 35 S. Xie, X. Zhang, D. Xiao, M. C. Paaui, J. Huang and M. M. F. Choi, *J. Phys. Chem. C*, 2011, **115**, 9943.
- 36 W. Song, J. Wang, Z. Mao, W. Xu and B. Zhao, *Spectrochim. Acta, Part A*, 2011, **79**, 1247.
- 37 M. V. Cañamares, J. V. Garcia-Ramos, J. D. Gómez-Varga, C. Domingo and S. Sanchez-Cortes, *Langmuir*, 2005, **21**, 8546.
- 38 S. Malynych, I. Luzinov and G. Chumanov, *J. Phys. Chem. B*, 2002, **106**, 1280.
- 39 P. Hildebrandt and M. Stockburger, *J. Phys. Chem.*, 1984, **88**, 5935.
- 40 P. C. Lee and D. Meisel, *J. Phys. Chem.*, 1982, **86**, 3391.
- 41 C. H. Munro, W. E. Smith, M. Garner, J. Clarkson and P. C. White, *Langmuir*, 1995, **11**, 3712.
- 42 T. A. Witten, Jr and L. M. Sander, *Phys. Rev. Lett.*, 1981, **47**, 1400.
- 43 X. Sun, L. Lin, Z. Li, Z. Zhang and J. Feng, *Mater. Lett.*, 2009, **63**, 2306.
- 44 Y. Han, R. Lupitskyy, T.-M. Chou, C. M. Stafford, H. Du and S. Sukhishvili, *Anal. Chem.*, 2011, **83**, 5873.
- 45 W. Ye, C. Shen, J. Tian, C. Wang, L. Bao and H. Gao, *Electrochem. Commun.*, 2008, **10**, 626.
- 46 G. D. Sulka and M. Jaskula, *Electrochim. Acta*, 2006, **51**, 6111.
- 47 F. J. Garcia-Vidal and J. B. Pendry, *Phys. Rev. Lett.*, 1996, **77**, 1166.
- 48 H. Shen, L. Stordrange, R. Manne, O. M. Kvalheim and Y. Liang, *Chemom. Intell. Lab. Syst.*, 2000, **51**, 37.
- 49 R. Goodacre, É. M. Timmins, R. Burton, N. Kaderbhai, A. M. Woodward, D. B. Kell and P. J. Rooney, *Microbiology*, 1998, **144**, 1157.